Nonlinear gravitational-wave interactions in an expanding universe

Fan Zhang,[1,2] Lee Lindblom,[3] and Zhi-Peng Peng[2,4]

[1]*Institute for Frontiers in Astronomy and Astrophysics, Beijing Normal University, Beijing 102206, China*
[2]*School of Physics and Astronomy, Beijing Normal University, Beijing 100875, China*
[3]*Department of Physics, Center for Dark Cosmology and Gravitation, University of California at San Diego, La Jolla, California 92093, USA*
[4]*School of Physics and Advanced Energy, Henan University of Technology, Henan 450001, China*

(Received 9 March 2026; accepted 16 July 2026; published 14 August 2026)

This study explores the nonlinear interactions between gravitational waves in an expanding universe. Random ensembles of gravitational waves are evolved numerically in cosmological models whose spatial volumes increase by more than an order of magnitude during these simulations. These evolutions show the spectra of the gravitational waves evolving as energy cascades away from the wavelengths at the peak of the initial spectra toward both longer and shorter wavelengths. Evolutions performed at different gravitational-wave amplitudes are shown to produce cascades that scale with amplitude in the way predicted by the four-wave scattering models of gravitational-wave turbulence.

DOI: 10.1103/cbzd-3qvf

I. INTRODUCTION

Gravitational waves are fluctuations in the geometry of spacetime that propagate at the speed of light according to Einstein's general relativity theory. It has long been assumed that the nonlinearity of Einstein's equation could in suitable circumstances lead to interactions between these waves which lead to turbulent cascades that transform their spectra. These nonlinear interactions were studied first in the context of anti–de Sitter spacetime. Using both numerical and analytical methods, the studies reported in Refs. [1,2] found that a turbulent cascade of gravitational waves from lower to higher frequencies could drive an instability in anti–de Sitter spacetime. Those studies speculate that this instability could result in the production of black holes. The studies reported in Refs. [3,4] have also found, using analytical and numerical methods, that inverse turbulent cascades of gravitational waves from higher to lower frequencies could occur in the gravitational waves emitted by perturbed black holes.

Several studies have considered the question whether gravitational-wave turbulence could be playing a role in the evolution of our Universe; e.g., Refs. [5–10]. The most fundamental of these studies, Refs. [5,6,9], used analytical methods to show that gravitational waves in general relativity theory can exhibit turbulent behavior leading to energy transfers from lower to higher frequency waves, and inverse transfers from higher to lower frequencies under suitable circumstances. The issue of whether such turbulent cascades play a role in our Universe is still an open question. The analysis in Ref. [7] showed that the expansion time in our Universe is shorter than the estimated growth time needed to establish a turbulent cascade, suggesting that gravitational-wave turbulence does not play an important role in our Universe. A different analysis in Ref. [8] suggests that an inverse cascade from higher to lower frequency gravitational waves could drive an inflation epoch in our early Universe. Those gravitational-wave turbulence studies have all been analytical. A recent study however, Ref. [10], has reported the development and testing of numerical methods that may soon allow some of these questions to be explored in ways that are not amenable to analytical methods.

This paper presents the results of fully nonlinear three-dimensional numerical evolutions of gravitational waves in expanding cosmological models. The initial data for these evolutions were constructed on spatial hypersurfaces with the topology of the three-torus. The initial data used in this study include an ensemble of gravitational waves (constructed using the appropriate transverse-traceless tensor harmonics on the three-torus) having random phases and a spectrum that peaks for wavelengths half the size of the universe. Initial data were constructed for ensembles of gravitational waves with three different dimensionless amplitude scales, $\mathcal{A}_s = \{0.001, 0.01, 0.1\}$, so that the effects of nonlinearity could be assessed. The methods used to construct these initial data are described in detail in Sec. II. The properties of the transverse-traceless tensor harmonics on the three-torus are summarized in Appendix A.

A covariant symmetric-hyperbolic representation of Einstein's vacuum equation is used in this study to evolve these initial data until the spatial volumes of the solutions have expanded by at least an order of magnitude. The numerical methods used to solve these evolution equations are described in some detail in Sec. III. This section presents visualizations of some of the results and demonstrates that the numerical evolutions presented here are numerically convergent. Details of the covariant symmetric-hyperbolic representation of Einstein's equation are summarized in Appendixes B and C.

The evolution of the spectra of the gravitational waves in these numerical solutions are examined in Sec. IV. These results show clear evidence for the transfer of energy from longer wavelengths into shorter-wavelength gravitational waves, and thus evidence for the initial stages of a standard turbulent cascade. These results also show some evidence for an inverse cascade of energy from higher- to lower-frequency gravitational waves. The implications of these results are discussed in Sec. V. For example, it is shown that the amplitudes of the gravitational waves created by these turbulent cascades scale with the amplitude in precisely the way predicted by the four-wave scattering models of gravitational-wave turbulence. The more subtle evidence produced by this study for the existence of an inverse cascade of energy from higher- to lower-frequency gravitational waves is also discussed in Sec. V.

II. INITIAL DATA

Solutions to Einstein's equation are constructed for this study by evolving suitable initial data specified on a spacelike hypersurface. The required initial data consist of the metric g_{ij} and extrinsic curvature K_{ij} of that initial hypersurface. (The tensor indices $i, j, \ldots$ range over the three coordinates on each $t = \text{constant}$ hypersurface.) Certain components of the Einstein equation are constraints on these fields, generally referred to as the Hamiltonian and momentum constraints. For a vacuum spacetime, these constraint equations are given by [11]

$$R + K^2 - K_{ij}K^{ij} = 0, \tag{1}$$

$$D^j(g_{ij}K - K_{ij}) = 0. \tag{2}$$

Here, $R = g^{ij}R_{ij}$ is the trace of the Ricci tensor determined by the spatial metric g_{ij}, $K = g^{ij}K_{ij}$ the trace of the extrinsic curvature, and D_i the covariant derivative compatible with g_{ij}: $D_m g_{ij} = 0$.

This study is focused on the interactions among an ensemble of gravitational waves in an expanding universe. The initial data representing these waves are constructed for this study by solving Eqs. (1) and (2) using the constant mean curvature form of the conformal initial value problem; see, e.g., Refs. [11,12]. In this approach, the trace of the extrinsic curvature K is assumed to be constant on the initial hypersurface. In this case, the spatial metric g_{ij} and extrinsic curvature K_{ij} can be expressed in terms of the conformal fields φ, e_{ij}, and A_{ij}:

$$g_{ij} = \varphi^4 e_{ij}, \tag{3}$$

$$K_{ij} = \frac{1}{3}\varphi^4 e_{ij}K + \varphi^{-2}A_{ij}, \tag{4}$$

where e_{ij} is the conformal metric, φ the conformal factor, and A_{ij} the transverse-traceless part of the extrinsic curvature. The momentum constraint forces the longitudinal part of the trace-free extrinsic curvature to vanish on the compact spatial hypersurfaces used in this study [12].

The conformal metric e_{ij} can be chosen freely in this version of the initial value problem. The compact orientable cosmological models studied here are constructed on manifolds with spatial hypersurfaces with the topology of the three-torus T^3. Therefore, the conformal metric e_{ij} can be chosen to be the flat Euclidean metric. This study represents T^3 using periodic Cartesian coordinates, and in these coordinates e_{ij} is just the identity matrix $e_{ij} = \delta_{ij}$. The notation ∂_m is used for the covariant derivative compatible with the Euclidean metric $\partial_m e_{ij} = 0$, which is just the partial derivative in Cartesian coordinates.

The transverse-traceless extrinsic curvature A_{ij} can also be chosen freely in this version of the initial value problem. The tensor harmonics $Y^{+}_{ij,\mathbf{k}}$ and $Y^{\times}_{ij,\mathbf{k}}$ provide a complete basis for the symmetric transverse-traceless tensors on T^3 [13]. Therefore, any symmetric transverse-traceless tensor, including A_{ij}, can be written as a linear combination of these harmonics:

$$A_{ij} = \Re\left\{\sum_{\vec{k}}\left[\mathcal{A}^{+}_{\mathbf{k}} Y^{+}_{ij,\vec{k}} + \mathcal{A}^{\times}_{\mathbf{k}} T^{\times}_{ij,\vec{k}}\right]\right\}, \tag{5}$$

where $\mathcal{A}^{+}_{\mathbf{k}}$ and $\mathcal{A}^{\times}_{\mathbf{k}}$ are complex constants that represent the spectra of the gravitational waves that contribute to A_{ij}. Explicit expressions for, and the properties of, these tensor harmonics are given in Appendix A.

The extrinsic curvature K_{ij} is the Lie derivative of the spatial metric along the timelike normals to the initial hypersurface, and (roughly speaking) A_{ij} represents the time derivative of the propagating gravitational-wave degrees of freedom of the metric. The tensor harmonics $Y^{+}_{ij,\mathbf{k}}$ and $Y^{\times}_{ij,\mathbf{k}}$ multiplied by $e^{i2\pi\kappa t}$, where $\kappa^2 = |\mathbf{k}|^2 = k_x^2 + k_y^2 + k_z^2$, are solutions to the linearized Einstein equation that represent small-amplitude gravitational-wave perturbations on a flat T^3. The amplitudes of the tensor harmonics $\mathcal{A}^{+}_{\mathbf{k}}$ and $\mathcal{A}^{+}_{\mathbf{k}}$ that determine A_{ij} are therefore $2\pi\kappa$ times the amplitudes of these gravitational-wave perturbations. The spectrum of amplitudes chosen for this study are given by

$$\mathcal{A}^{+}_{\mathbf{k}} = 2\pi\kappa\mathcal{A}_s f(\kappa)e^{i\Psi^{+}_{\mathbf{k}}}, \tag{6}$$

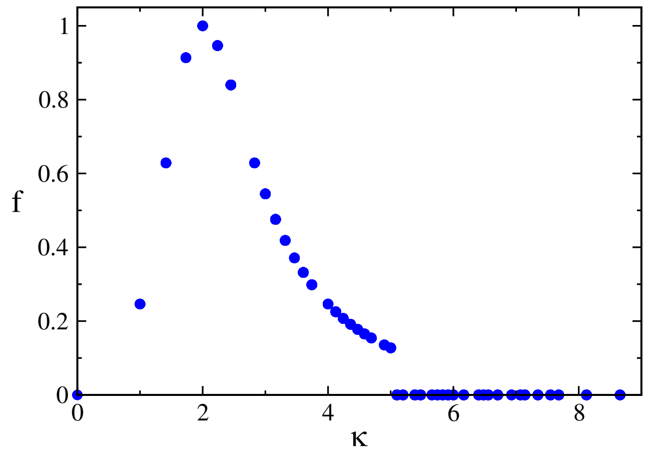

FIG. 1. The function $f(\kappa)$ describes the amplitudes of the gravitational-wave perturbations used to construct the initial data. Each point represents the amplitude used for the collection of gravitational-wave modes with $\kappa^2 = |\mathbf{k}|^2 = k_x^2 + k_y^2 + k_z^2$, where k_x, k_y, k_z are integers in the ranges $-5 \le k_i \le 5$.

$$\mathcal{A}^\times_{\mathbf{k}} = 2\pi\kappa\mathcal{A}_s f(\kappa) e^{i\Psi^\times_{\mathbf{k}}}, \tag{7}$$

where $f(\kappa)$ determines the spectra of the initial gravitational-wave ensemble, $\mathcal{A}_s$ determines the overall amplitude scale of the ensemble, and $0 \le \Psi^+_{\mathbf{k}} \le 2\pi$ and $0 \le \Psi^\times_{\mathbf{k}} \le 2\pi$ are randomly chosen phase parameters. The spectral function $f(\kappa)$ used in this study has the form

$$f(\kappa) = \frac{16\kappa^3}{64 + \kappa^6} \tag{8}$$

for $\kappa \le 5$ and $f(\kappa) = 0$ for $\kappa > 5$. This conformal initial spectrum $f(\kappa)$, which peaks at the wavelength equal to half the size of the three-torus initial surface, is illustrated in Fig. 1.

When expressed in terms of the conformal fields defined in Eqs. (3) and (4), the momentum constraint Eq. (2) is automatically satisfied for any transverse-traceless A_{ij}, and therefore for any A_{ij} given by Eq. (5). The Hamiltonian constraint Eq. (1) becomes an elliptic partial differential equation that determines the conformal factor φ:

$$\partial^m\partial_m\varphi = \frac{1}{12}K^2\varphi^5 - \frac{1}{8}A_{ij}A^{ij}\varphi^{-7}. \tag{9}$$

The integral of the left side of Eq. (9) vanishes on the T^3 initial hypersurface used in this study, so the integral of the right side must also vanish, which implies

$$K^2 \int \varphi^5 d^3x = \frac{3}{2}\int A_{ij}A^{ij}\varphi^{-7} d^3x. \tag{10}$$

This condition determines K as a function of the conformal factor and must be imposed together with Eq. (9) to determine φ.

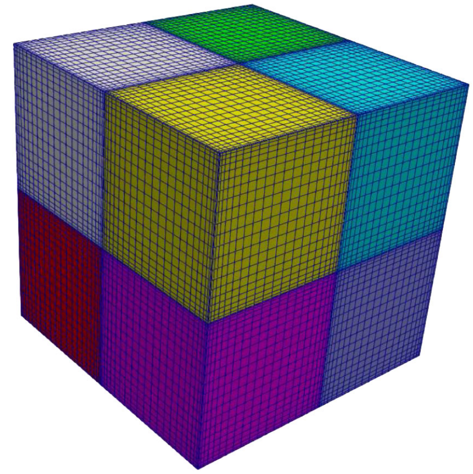

FIG. 2. This figure illustrates the computational domain used in this study. The tree-torus topology is implemented by identifying points on the opposite faces of the cubic domain, which is subdivided into eight smaller cubic subdomains. The pseudospectral grid is illustrated here for the lowest resolution used in this study, with $N = 24$ grid points in each direction in each subdomain.

The solutions to these equations are found numerically for this study using the pseudospectral methods implemented in the SpEC numerical relativity code (developed initially by the Caltech and Cornell numerical relativity groups) [14,15]. These numerical solutions are carried out in SpEC using the KSP linear and the SNES nonlinear solvers from the PETSC software library [16]. These methods solve the nonlinear Eq. (9) iteratively by minimizing a sequence of discrete versions of the residual $\mathcal{E}_{(n)}$ defined by

$$\mathcal{E}_{(n)} = \partial^m\partial_m\varphi_{(n)} - \frac{1}{12}K^2_{(n-1)}\varphi^5_{(n)} + \frac{1}{8}A_{ij}A^{ij}\varphi^{-7}_{(n)}, \tag{11}$$

where $\varphi_{(n)}$ is the function that minimizes $\mathcal{E}_{(n)}$, and $K_{(n-1)}$ is determined by Eq. (10) using $\varphi_{(n-1)}$ from the previous iteration. The calculations were initiated in this study by setting $\varphi_{(0)} = 1$, then computing $K_{(0)}$ from Eq. (10), and iterating the process until convergence of the minimized $\mathcal{E}_{(n)}$ was achieved.

The numerical computations for this study were carried out on the cubic computational domain illustrated in Fig. 2. The three-torus topology of this domain is implemented by imposing boundary conditions that identify points on the opposite faces of the cubic domain. The computations on this domain are subdivided into the eight cubic subdomains shown in Fig. 2 for computational efficiency and to achieve higher resolutions. Pseudospectral grids are constructed on each subdomain with N collocation points in each spatial dimension in each subdomain.

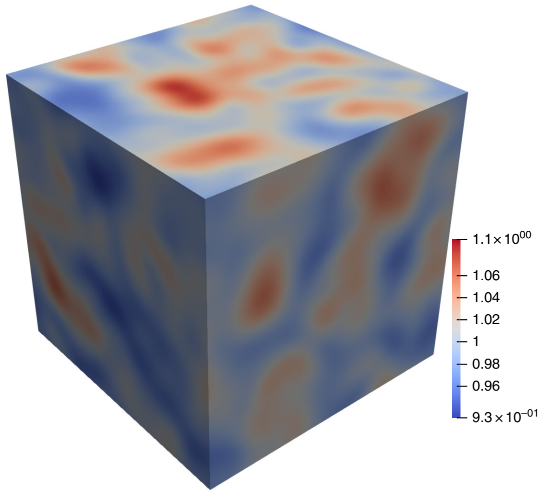

FIG. 3. This figure illustrates the solution of the initial value problem φ for the gravitational-wave amplitude scale $\mathcal{A}_s = 0.1$ case.

Computations for this study were carried out on grids with resolutions $N = \{24, 32, 40, 48\}$.

The initial value Eqs. (9) and (10) were solved for this study using gravitational-wave data having three different amplitude scales: $\mathcal{A}_s = \{0.001, 0.01, 0.1\}$. Figure 3 illustrates φ for the solution with gravitational-wave amplitude $\mathcal{A}_s = 0.1$ and spatial resolution $N = 48$. Solutions for the other gravitational-wave amplitudes have similar structures, but smaller variations away from unity.

The accuracy of the solutions to the initial value equations computed for this study were measured by evaluating a norm of the Hamiltonian constraint $\langle\mathcal{H}\rangle$ defined by

$$\langle\mathcal{H}\rangle^2 = \frac{1}{\mathcal{V}}\int \sqrt{\det g}(R + K^2 - K_{ij}K^{ij})^2 d^3x, \qquad (12)$$

where the spatial volume $\mathcal{V}$ of the spacelike hypersurface was determined by the integral

$$\mathcal{V} = \int \sqrt{\det g}\, d^3x. \qquad (13)$$

On the initial hypersurface, the expression for the volume $\mathcal{V}(0)$ reduces in Cartesian coordinates to the expression

$$\mathcal{V}(0) = \int \varphi^6 d^3x, \qquad (14)$$

which depends (weakly) on the gravitational-wave amplitude scale $\mathcal{A}_s$. The solutions to the initial value equations with different gravitational-wave scales also result in different values for the trace of the extrinsic curvature K. The resulting extrinsic curvatures are roughly proportional to the wave amplitude scale $\mathcal{A}_s$, so the expansion rates of the spacetimes for the different cases differ by comparable amounts.

TABLE I. The initial extrinsic curvatures K, spatial volumes $\mathcal{V}$, and norms of Hamiltonian constraint $\langle\mathcal{H}\rangle$ for the highest-resolution solutions to Eqs. (9) and (10) for the gravitational-wave amplitude scales $\mathcal{A}_s$ included in this study. (This study uses the Ref. [17] sign convention for the extrinsic curvature K in which $K < 0$ corresponds to expansion.).

$\mathcal{A}_s$	$\langle\mathcal{H}\rangle$	$\mathcal{V}(0)$	K
0.001	3.45×10^{-9}	1.000004	−0.21194
0.01	3.64×10^{-8}	1.000461	−2.11445
0.1	2.51×10^{-7}	1.022513	−20.0228

The resulting values of the Hamiltonian constraint norms $\langle\mathcal{H}\rangle$, the initial volumes $\mathcal{V}(0)$, and the trace of the extrinsic curvature K are given in Table I for the different gravitational-wave amplitude scales $\mathcal{A}_s$ included in this study. These results are for the highest-resolution solutions from each gravitational-wave scale $\mathcal{A}_s$ ($N = 40$ for $\mathcal{A}_s = 0.001$ and $N = 48$ for $\mathcal{A}_s = 0.01$ and $\mathcal{A}_s = 0.1$).

III. SPACETIME EVOLUTIONS

The representation of the Einstein evolution equation used in this study is the covariant first-order symmetric-hyperbolic representation developed in Ref. [18], whose salient features are summarized in Appendix C. The dynamical fields in this representation are the spacetime metric ψ_{ab}, its time derivative $\Pi_{ab} = -t^c\tilde{\nabla}_c\psi_{ab}$, and its spatial derivatives $\Phi_{iab} = \tilde{\nabla}_i\psi_{ab}$, where t^c is the future directed timelike unit normal to the $t =$ constant hypersurfaces. The indices from the first part of the alphabet, e.g., $a, b, c, \ldots$, range over the four-dimensional spacetime coordinates, while the indices from the later parts of the alphabet, e.g., $i, j, \ldots$, range over the three-dimensional spatial coordinates on each $t =$ constant hypersurface.

The covariant derivative $\tilde{\nabla}_a$ used in the definitions of the first-order dynamical fields is the one compatible with a time-independent reference metric $\tilde{\psi}_{ab}$: $\tilde{\nabla}_c\tilde{\psi}_{ab} = 0$. Another essential use of this reference metric is the construction of the mappings that enforce the appropriate boundary conditions at the interfaces between the cubic regions that serve as coordinate charts on the spacelike hypersurfaces [18,19]. The spacetimes included in this study have spacelike hypersurfaces with three-torus topologies. Therefore, a natural choice for the reference metric in this case is the flat Minkowski metric

$$d\tilde{s}^2 = \tilde{\psi}_{ab}dx^a dx^b = -dt^2 + e_{ij}dx^i dx^j. \qquad (15)$$

In this study, the reference covariant derivative is written as $\tilde{\nabla}_a = \partial_a$ since it reduces to partial derivatives in Cartesian coordinates.

The spatial metrics g^0_{ij} produced by the solutions to the Einstein constraint equations described in Sec. II are used to construct the initial data for the spacetime metric ψ^0_{ab}:

$$ds^2 = \psi^0_{ab} dx^a dx^b = -dt^2 + g^0_{ij}\, dx^i dx^j. \tag{16}$$

The values of the other dynamical fields on the initial hypersurface are given by

$$\Pi^0_{ta} = 0, \tag{17}$$

$$\Pi^0_{ij} = 2K^0_{ij}, \tag{18}$$

$$\Phi^0_{iab} = \partial_i \psi^0_{ab}, \tag{19}$$

where K^0_{ij} is the physical extrinsic curvature determined from the solution to the initial value equations in Sec. II. A more complete discussion of the relationship between the first-order dynamical fields ψ_{ab}, Π_{ab}, Φ_{iab}, and the more standard three-plus-one dynamical fields g_{ij} and K_{ij} is given in Appendix B.

The covariant symmetric-hyperbolic representation of the Einstein evolution equation used in this study has been implemented in the SpEC numerical relativity code [18]. This code has been tested by performing fully nonlinear evolutions of small-amplitude gravitational-wave ensembles propagating in the Einstein static universe [18]. Those tests demonstrated high-precision numerical convergence and long-term numerical stability for the evolutions lasting about 160 light-crossing times of the three-sphere spatial slices. This code has also been tested by performing evolutions of expanding homogeneous and nonhomogeneous cosmological models on manifolds with spatial slices having nonorientable topologies [20]. These nonorientable cosmological model tests were shown to be numerically convergent for the evolutions lasting long enough to increase their spatial volumes by a factor of 10.

The numerical evolutions for this study were carried out using the initial data constructed in Sec. II with gravitational-wave ensembles having amplitude scales $\mathcal{A}_s = \{0.001, 0.01, 0.1\}$, on computational grids with spatial resolutions $N = \{24, 32, 40, 48\}$ in each direction in each of the eight cubic regions. The time integrations for the evolutions in the present study were carried out using an eighth-order Dormand-Prince adaptive time step integrator [21] that is part of the SpEC numerical relativity code. The time step error tolerance was set at $10^{-5-N/16}$ (where N is the spatial resolution) for the evolutions completed for this study.

The goal of this study was to evolve initial data for ensembles of gravitational waves until changes from the initial gravitational-wave spectra could be observed. To accomplish this goal, the evolutions were carried out until the volumes of the spatial hypersurfaces of the spacetime models grew by at least an order of magnitude. The initial expansion rates for these spacetime models are set by the initial values of the trace of the extrinsic curvature K^0. The values of K^0 from Table I are roughly inversely proportional to the gravitational-wave amplitude scales $\mathcal{A}_s$. Consequently, the coordinate time evolutions required to achieve the desired volume growths also need to be inversely proportional to $\mathcal{A}_s$. These considerations determined the coordinate time intervals for the evolutions in this study: $0 \le t \le 0.1$ for the $\mathcal{A}_s = 0.1$ case, $0 \le t \le 1.0$ for $\mathcal{A}_s = 0.01$, and $0 \le t \le 10.0$ for $\mathcal{A}_s = 0.001$. Figure 4 illustrates the evolution of the physical volumes of the $t =$ constant spacelike hypersurfaces $\mathcal{V}(t)$ defined in Eq. (13) for these cases.

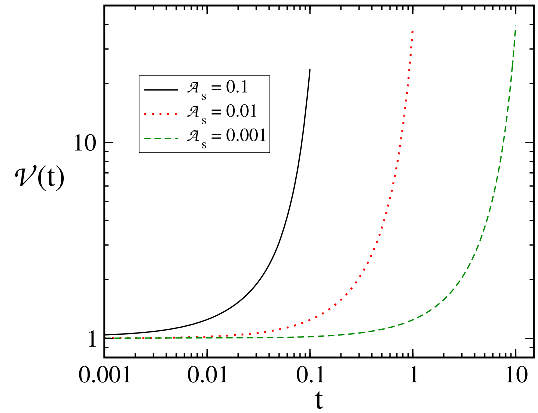

FIG. 4. This figure illustrates the volumes $\mathcal{V}(t)$ defined in Eq. (13) for the evolutions with gravitational-wave amplitude scales $\mathcal{A}_s = \{0.001, 0.01, 0.1\}$.

The evolution of the gravitational-wave spectra in these expanding cosmological models is explored quantitatively in some detail in Sec. IV. A more qualitative approach is taken here using the Weyl tensor, which is the traditional geometrical tool for studying the properties of gravitational waves in vacuum spacetimes. An impression of the evolution of the gravitational-wave spectra in these models can be obtained by visualizing the curvature scalar

$$\mathcal{W}^2 = \frac{1}{16} |C_{abcd} C^{abcd}|, \tag{20}$$

where C_{abcd} is the Weyl tensor. Figures 5 and 6 illustrate $\mathcal{W}$ on the surfaces of the computational domain for the evolution of the gravitational-wave ensemble with amplitude scale $\mathcal{A}_s = 0.1$. Figure 5 shows $\mathcal{W}$ at the initial coordinate time $t = 0$ and Fig. 6 at the final time $t = 0.1$. These figures show that the overall pattern of gravitational-wave-induced curvature evolves toward shorter wavelengths and more overall spatial uniformity during the course of this evolution.

The first-order symmetric-hyperbolic representation of the Einstein system has a large number of constraints, which are described in some detail in Appendix C. The overall magnitude of constraint violations is summarized

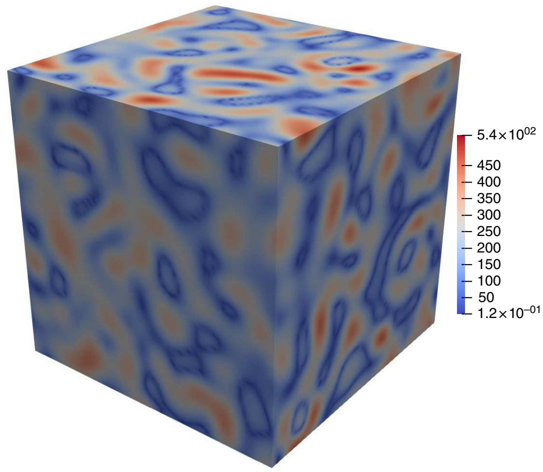

FIG. 5. This figure illustrates the Weyl curvature scalar $\mathcal{W}$ defined in Eq. (20) at time $t = 0$ for the evolution of the gravitational-wave ensemble with amplitude scale $\mathcal{A}_s = 0.1$.

by the scalar $\mathcal{C}_\psi$, defined in Eq. (C12), that vanishes if and only if all the constraints are satisfied. The dimensionless norm of this quantity $\|\mathcal{C}_\psi\|$ defined in Eq. (C13) provides a useful measure of the fractional constraint violation errors in the cosmological models produced by these evolutions. Figures 7–9 show $\|\mathcal{C}_\psi\|(t)$ for the evolutions of the initial data with gravitational-wave amplitude scales $\mathcal{A}_s = \{0.001, 0.01, 0.1\}$, respectively. These graphs show that the numerical methods used in this study are convergent as the resolution N of the computational grid is increased.

The evolutions of the $\mathcal{A}_s = 0.001$ initial data have significantly lower constraint violation norms $\|\mathcal{C}_\psi\|(t)$ than the $\mathcal{A}_s = \{0.01, 0.1\}$ evolutions. Therefore, the highest-resolution $N = 48$ evolution for the $\mathcal{A}_s = 0.001$ case was not included in this study. The higher-resolution evolutions of the $\mathcal{A}_s = 0.001$ initial data also show significant variations in $\|\mathcal{C}_\psi\|(t)$ at early times. The time stepping error thresholds used in these runs were the same as those used in the $\mathcal{A}_s = \{0.01, 0.1\}$ evolutions which have higher

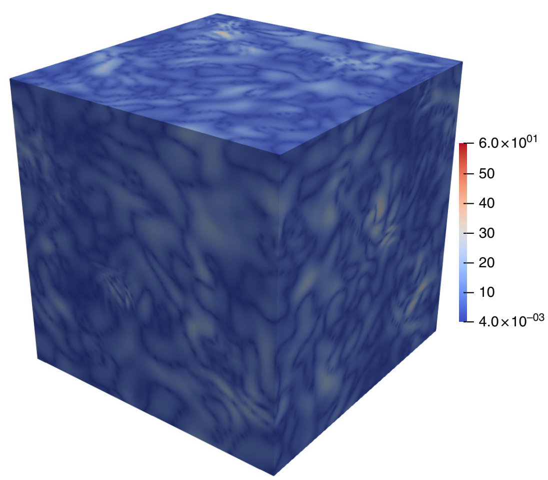

FIG. 6. This figure illustrates the Weyl curvature scalar $\mathcal{W}$ defined in Eq. (20) at the final time $t = 0.1$ for the evolution of the gravitational -wave ensemble with amplitude scale $\mathcal{A}_s = 0.1$.

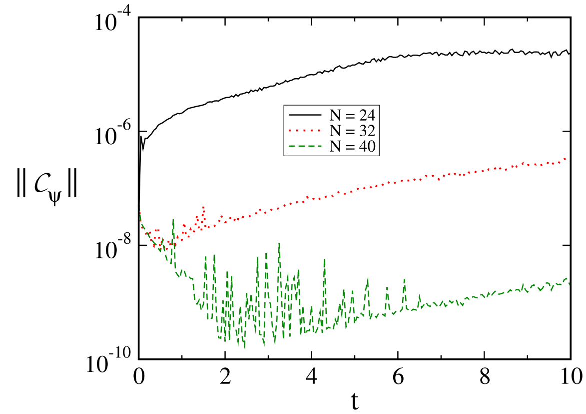

FIG. 7. This figure illustrates the constraint norms $\|\mathcal{C}_\psi\|$ defined in Eq. (C13) for the $\mathcal{A}_s = 0.001$ evolutions.

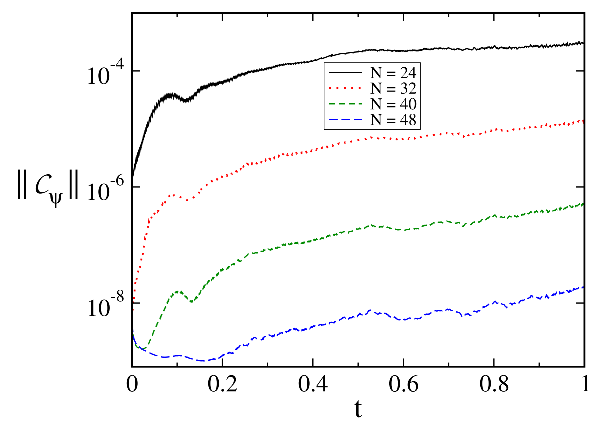

FIG. 8. This figure illustrates the constraint norms $\|\mathcal{C}_\psi\|$ defined in Eq. (C13) for the $\mathcal{A}_s = 0.01$ evolutions.

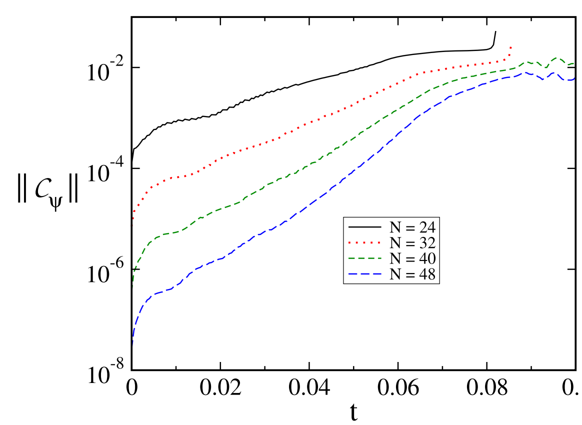

FIG. 9. This figure illustrates the constraint norms $\|\mathcal{C}_\psi\|$ defined in Eq. (C13) for the $\mathcal{A}_s = 0.1$ evolutions.

overall constraint violation levels. It is possible that these higher-resolution $\mathcal{A}_s = 0.001$ evolutions could have been improved somewhat by reducing their time stepping error thresholds. This was not done because reducing those tolerances would cost considerable additional computer time, and the overall level of constraint violations in the runs presented here were considered to be sufficiently small for the purposes of this study.

IV. SPECTRAL EVOLUTIONS

The spectra of the gravitational waves change in various ways as the cosmological models evolve. The most basic effect is the redshifting of these waves as the spacetimes expand. The focus of this study, however, is the more subtle effects on these spectra caused by the nonlinear interactions between the gravitational waves. These redshift-independent effects can be extracted from the dynamical gravitational fields by expanding those fields in harmonic basis functions tied to the topology rather than the geometry of the spatial hypersurfaces. The coefficients of the harmonic basis functions in these expansions provide spectra that are independent of the size of the universe and are therefore independent of the redshift of those waves. The evolution of the gravitational-wave spectra measured in this way are caused by interactions between the gravitational waves rather than the overall expansion of the universe.

The transverse-traceless parts of the extrinsic curvature of the $t =$ constant hypersurfaces K_{ij} are directly affected by the gravitational-wave degrees of freedom of the spacetime geometry. The initial data constructed in Sec. II used this fact to insert gravitational waves with a specified spectrum into the dynamical fields that determine the spacetime geometry. The evolution of these spectra is studied here by expanding the $K_{ij}(t)$ determined by the Einstein evolution equations in a suitable basis of transverse tensor harmonics. The primary dynamical fields used in this study are the fields $\psi_{ab}(t)$, $\Pi_{ab}(t)$, and $\Phi_{iab}(t)$ described in Sec. III. The extrinsic curvatures $K_{ij}(t)$ are (somewhat complicated) algebraic functions of the primary dynamical fields that are described in some detail in Appendix B.

The $t =$ constant spatial hypersurfaces of the spacetime models included in this study have the topology of the three-torus. Therefore, the three-torus transverse-traceless tensor harmonics $Y^{+}_{ij,\mathbf{k}}$ and $Y^{\times}_{ij,\mathbf{k}}$ developed in Ref. [13] are the appropriate ones to represent the gravitational-wave degrees of freedom in K_{ij}. Detailed expressions for these harmonics are given in Appendix A. The tensor harmonics $Y^{+}_{ij,\mathbf{k}}$ and $Y^{\times}_{ij,\mathbf{k}}$ form a complete basis for the symmetric transverse-traceless tensors on the three-torus [13]. Therefore, without loss of generality the transverse traceless parts of the time evolving extrinsic curvature $K_{ij}(t)$ can be represented using them. The spectral coefficients $\mathcal{K}^{p}_{\mathbf{k}}$

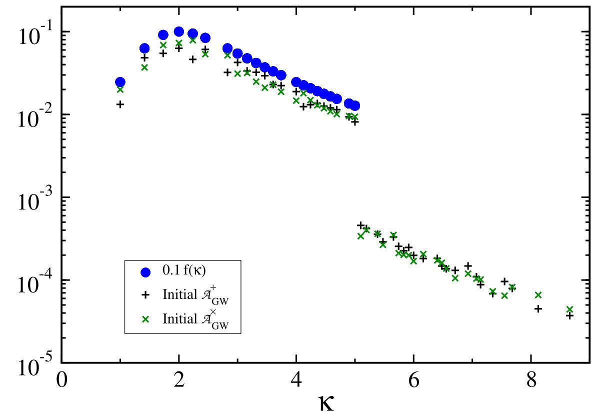

FIG. 10. This figure compares the gravitational-wave spectrum extracted from the $\mathcal{A}_s = 0.1$ physical initial data with the spectrum of the conformal initial data $0.1f(\kappa)$ used to construct that physical data.

that describe the gravitational-wave degrees of freedom of the extrinsic curvature are determined by the integrals

$$\mathcal{K}^{p}_{\mathbf{k}}(t) = \int e^{ij} e^{mn} K_{im}(t) Y^{p*}_{jn,\mathbf{k}} d^3x. \tag{21}$$

These extrinsic curvature spectral coefficients are converted to effective metric perturbation coefficients by dividing by $2\pi\kappa$, in analogy with the initial data construction in Eqs. (6) and (7). The angle-averaged gravitational-wave spectrum $\mathcal{A}^{p}_{\mathrm{GW}}(\kappa)$ is then obtained by averaging these spectral coefficients over the tensor-harmonic modes with parameters $\mathbf{k}$ having length $\kappa^2 = |\mathbf{k}|^2 = k_x^2 + k_y^2 + k_z^2$:

$$[\mathcal{A}^{p}_{\mathrm{GW}}(\kappa)]^2 = \frac{\sum_{\kappa=|\mathbf{k}|} \mathcal{K}^{p}_{\mathbf{k}}(t)\mathcal{K}^{p*}_{\mathbf{k}}(t)}{4\pi^2\kappa^2 M(\kappa)}, \tag{22}$$

where $M(\kappa)$ is the total number of gravitational-wave modes with $|\mathbf{k}| = \kappa$.

Figure 10 illustrates the gravitational-wave amplitudes $\mathcal{A}^{+}_{\mathrm{GW}}(\kappa)$ and $\mathcal{A}^{\times}_{\mathrm{GW}}(\kappa)$ for the $t = 0$ initial data with amplitude scale $\mathcal{A}_s = 0.1$. For comparison, this figure also shows $\mathcal{A}_s f(\kappa)$ that defined the gravitational-wave amplitudes in the conformal extrinsic curvature. This comparison shows that in the long-wavelength domain where $f(\kappa) > 0$, the physical gravitational-wave amplitudes $\mathcal{A}^{p}_{\mathrm{GW}}(\kappa)$ are somewhat smaller than $\mathcal{A}_s f(\kappa)$. In the shorter-wavelength domain where $\kappa > 5$, the physical amplitudes include an exponentially decreasing tail that was not present in $\mathcal{A}_s f(\kappa)$. These differences between the initial $\mathcal{A}^{p}_{\mathrm{GW}}(\kappa)$ and $\mathcal{A}_s f(\kappa)$ are caused by the nonlinear process that determined the physical initial data by solving Eqs. (4), (9), and (10).

Figures 11–13 illustrate the evolution of the spectra of physical gravitational-wave amplitudes $\mathcal{A}^{p}_{\mathrm{GW}}(\kappa)$ by comparing these spectra at the initial times $t = 0$ with those

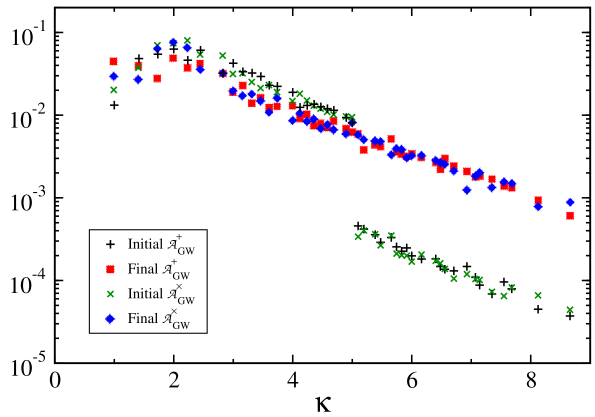

FIG. 11. This figure compares the initial and the final time gravitational-wave spectra extracted from the $\mathcal{A}_s = 0.1$ spacetime evolutions.

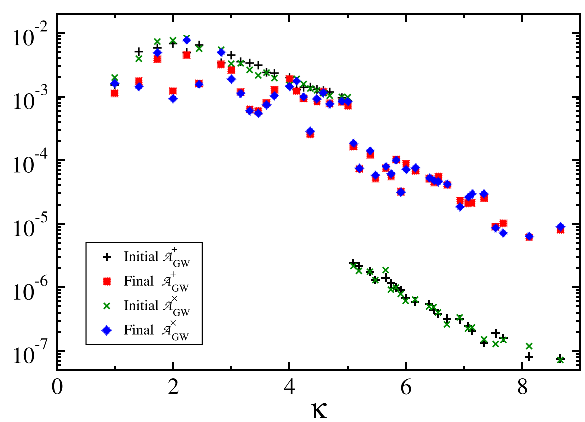

FIG. 12. This figure compares the initial and the final time gravitational-wave spectra extracted from the $\mathcal{A}_s = 0.01$ spacetime evolutions.

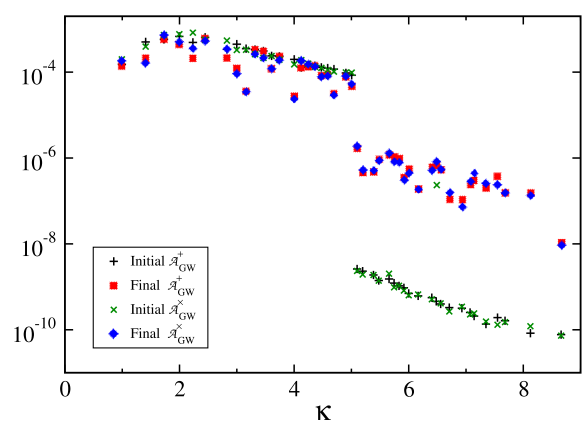

FIG. 13. This figure compares the initial and the final time gravitational-wave spectra extracted from the $\mathcal{A}_s = 0.001$ spacetime evolutions.

spectra at the final time in each evolution. These results show that in almost all of the long-wavelength range $\kappa \le 5$, the amplitudes at late times show modest decreases from their initial values. But in the shorter-wavelength range $\kappa > 5$, these results show significant amplification of the amplitudes at later times. This amplification is most pronounced in the evolution of the $\mathcal{A}_s = 0.1$ initial data shown in Fig. 11. Similar but less pronounced amplification is also seen in Figs. 12 and 13 for the $\mathcal{A}_s = 0.01$ and $\mathcal{A}_s = 0.001$ cases. The evolutions included in this study were evolved for the relatively short dynamical times needed for the volumes of these cosmological models to increase by somewhat more than a factor of 10. These results show that the nonlinear interactions between gravitational waves can cause significant modifications to the spectrum of these waves, even on the relatively short dynamical timescales of the simulations included in this study.

V. DISCUSSION

This study has demonstrated that nonlinear interactions among the gravitational waves in expanding cosmological models can be observed on fairly short dynamical timescales. The cosmological models constructed for this study were computed numerically by solving Einstein's evolution equations using initial data containing an ensemble of gravitational waves with different frequencies, propagation directions, and random phases. These spacetime models were evolved until the spatial volumes expanded by more than an order of magnitude. The initial data for these models were prepared with spectra peaked at wavelengths equal to half the size of their three-torus initial hypersurfaces. The evolved spectra at the ends of the evolutions in this study are shown in Figs. 11–13. These results clearly show that energy has been transferred from the longer-wavelength gravitational waves to shorter wavelengths as a result of a turbulent cascade in these evolutions. These results also suggest that the very longest-wavelength modes have been amplified by an inverse turbulent cascade.

Figure 14 compares the late-time gravitational-wave spectra $\mathcal{A}^{+}_{\mathrm{GW}}(\kappa)$ scaled by $1/\mathcal{A}_s^2$ for the evolutions with the three amplitude scales $\mathcal{A}_s = \{0.1, 0.01, 0.001\}$. This shows that the growth in the gravitational-wave energy density, which is proportional to the amplitudes squared $(\mathcal{A}^{+}_{\mathrm{GW}})^2$, is roughly proportional to $\mathcal{A}_s^4$ in the region where $\kappa > 5$. Virtually all of the gravitational-wave energy in this part of the spectrum was generated by nonlinear interactions between the waves. Therefore, the energy density in the region with $\kappa > 5$ is proportional to the dynamical-time duration of the evolutions in this study divided by the turbulent cascade timescale τ_{cas}. All the evolutions in this study were evolved for roughly the same dynamical time: the time needed for the volumes of the spatial slices to increase by about an order of magnitude. The invariance of the ratio $(\mathcal{A}^{+}_{\mathrm{GW}})^2/\mathcal{A}_s^4$ shown by the results in Fig. 14 therefore implies that the turbulence cascade timescale τ_{cas}

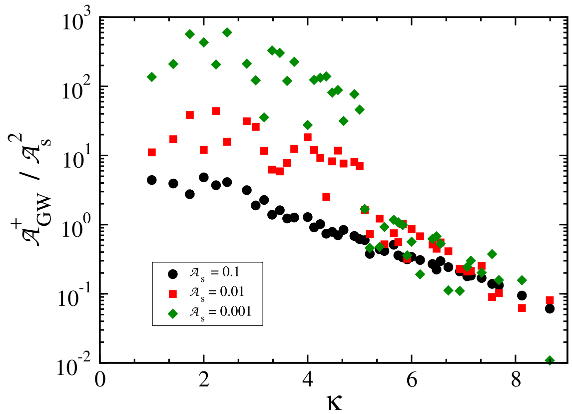

FIG. 14. This figure illustrates the ratio $\mathcal{A}^+_{\mathrm{GW}}/\mathcal{A}^2_s$ for late-time gravitational-wave spectra from the $\mathcal{A}_s = \{0.1, 0.01, 0.001\}$ evolutions. This shows that while the late-time amplitudes of the long-wavelength gravitational waves with $\kappa \le 5$ scale roughly linearly in $\mathcal{A}_s$, the short-wavelength waves with $\kappa > 5$ scale roughly quadratically in $\mathcal{A}_s$. The analogous figure for the $\times$ polarization is qualitatively similar.

TABLE II. The average extrinsic-curvature spectral coefficients $\mathcal{K}^+_0$ and $\mathcal{K}^\times_0$ for the $\kappa = 0$ modes are compared at the initial and final times for the evolutions of the initial data with gravitational-wave amplitude scales $\mathcal{A}_s = \{0.1, 0.01, 0.001\}$.

$\mathcal{A}_s$	t	$\mathcal{K}^+_0$	$\mathcal{K}^\times_0$
0.1	0.0	2.09×10^{-2}	1.89×10^{-2}
	0.1	1.84×10^{-1}	1.48×10^{-1}
0.01	0.0	1.09×10^{-4}	8.97×10^{-5}
	1.0	3.50×10^{-3}	1.98×10^{-3}
0.001	0.0	1.17×10^{-7}	9.39×10^{-8}
	10.0	5.28×10^{-6}	9.07×10^{-6}

observed in this study is proportional to $\mathcal{A}_s^{-4}$. This scaling agrees exactly with the expression for τ_{cas} obtained in the analysis of gravitational turbulence generated by nonlinear four-wave scattering in Ref. [6].

The initial spectrum in Fig. 1 was chosen to enhance the possibility that the cascade of gravitational-wave energies from longer to shorter wavelengths could be observed in this study. The results displayed in Figs. 11–13 show that this was a good choice for that purpose. The spectrum shown in Fig. 1 has only a small number of gravitational-wave modes with wavelengths shorter than its peak at $\kappa = 2$. Therefore, this initial spectrum was not an optimal choice for exploring an inverse cascade of gravitational waves from shorter to longer wavelengths [3,4,6]. Nevertheless, there are two results from this study that suggest the existence of an inverse cascade.

(1) A careful examination of the $\kappa = 1$ gravitational-wave amplitudes for the $\mathcal{A}_s = 0.1$ evolutions in Fig. 11 shows that the late-time amplitudes $\mathcal{A}^+_{\mathrm{GW}}$ and $\mathcal{A}^\times_{\mathrm{GW}}$ are larger than their initial values by factors of 2 or 3. This result is consistent with an expected inverse cascade. The random phase choices used to construct the initial data for this study appear to be responsible for the gravitational-wave amplitude scatter seen in Figs. 11–13. Unfortunately, this random scatter is too large to allow the inverse cascade to be seen clearly in any of the other gravitational-wave modes with $\kappa < 2$ included in this study.

(2) The $\kappa = 0$ spectral coefficients of the extrinsic curvature $\mathcal{K}^+_0$ and $\mathcal{K}^\times_0$ defined in Eq. (21) grow significantly during all the evolutions included in this study. These $\kappa = 0$ extrinsic-curvature spectral coefficients cannot be converted to gravitational-wave amplitudes using Eq. (22), so the results cannot be included in Figs. 11–13. Instead, the initial and final $\mathcal{K}^+_0$ and $\mathcal{K}^\times_0$ have been listed in Table II. These results are also consistent with an inverse cascade of gravitational-wave energy from higher to lower frequencies.

A visual comparison of the initial and final Weyl scalars in Figs. 5 and 6 for the $\mathcal{A}_s = 0.1$ evolution suggests that the gravitational-wave distribution becomes more spatially uniform as the spacetime evolves. But it seems unlikely that this apparent uniformity is caused by the growth of the lower-frequency modes via the mechanism suggested in Refs. [3,4].

The spectra at the ends of the evolutions seen in Figs. 11–13 have roughly exponential falloff in κ for $\kappa > 5$. The Komolgorov spectra for fully developed gravitational-wave turbulence would be a power law of the form $\sim\kappa^{-3/2}$ [6]. While the evolutions performed for this study could not be extended long enough to see fully developed turbulence, there is some indication that the exponential spectra seen in these results are flatter for the more fully evolved larger $\mathcal{A}_s$ cases. This might indicate that these spectra are evolving toward power-law forms as the turbulence becomes more fully developed.

The rapidly expanding spatial volumes $\mathcal{V}(t)$ seen in Fig. 4 might suggest that these evolutions are undergoing accelerated expansion or inflation. We do not believe this is the case. These expansions are not exponential, but instead have pole singularities of the form $\mathcal{V}(t) = \mathcal{V}(0)/(1 - t/T)^p$. For example, in the $\mathcal{A}_s = 0.1$ case a numerical fit with $T = 0.142124$ and $p = 2.59075$ is essentially indistinguishable from the numerical evolution. This type of behavior has been found to be caused by the harmonic gauge condition used for the time coordinates in other numerical studies of homogeneous cosmological models (see Refs. [20,22]). We believe that this harmonic gauge condition is responsible for the pole singularities in $\mathcal{V}(t)$ seen in the evolutions in this study as well.

ACKNOWLEDGMENTS

We thank Michael Holst for providing some of the computational resources used to perform this research. F. Z. was supported by the National Key Research and Development Program of China Grant No. 2023YFC2205801, and the National Natural Science Foundation of China Grants No. 12433001 and No. 12021003. L. L. was supported in part by Grant No. 2407545 from the National Science Foundation to the University of California at San Diego, USA. Z.-P. P. was supported by the Talent Introduction Fund Grant No. 2020BS035 at Henan University of Technology and the Natural Science Foundation of Henan Grant No. 232300421351.

DATA AVAILABILITY

There are no publicly available research data or software supporting this manuscript. Requests for further information or data should be sent to the authors.

APPENDIX A: TRANSVERSE-TRACELESS TENSOR HARMONICS ON THE THREE-TORUS

The three-torus can be represented using coordinates $x^n = \{x, y, z\}$ with ranges $0 \le x < 1$, $0 \le y < 1$, and $0 \le z < 1$, and periodic boundary conditions. These periodic Cartesian coordinates are in effect the ones used in the numerical computations performed for this study. The transverse-traceless three-torus tensor harmonics constructed in Ref. [13] are expressed in these periodic Cartesian coordinates:

$$Y^{+}_{ij,\mathbf{k}} = \frac{e^{i2\pi k_n x^n}}{\sqrt{2}}(\hat{\ell}_i\hat{\ell}_j - \hat{m}_i\hat{m}_j), \qquad \text{(A1)}$$

$$Y^{\times}_{ij,\mathbf{k}} = \frac{e^{i2\pi k_n x^n}}{\sqrt{2}}(\hat{\ell}_i\hat{m}_j + \hat{\ell}_j\hat{m}_i), \qquad \text{(A2)}$$

where the parameter $\mathbf{k} \neq 0$ is a vector

$$\mathbf{k} = k_n = \{k_x, k_y, k_z\}, \qquad \text{(A3)}$$

whose components $\{k_x, k_y, k_z\}$ are integers. The vectors $\hat{k}_i$, $\hat{\ell}_i$, and $\hat{m}_i$ form an orthonormal triad given by

$$\hat{k}_i = \frac{1}{\kappa}\{k_x, k_y, k_z\}, \qquad \text{(A4)}$$

$$\hat{\ell}_i = \frac{1}{\lambda}\{-k_y - k_z, k_x - k_z, k_x + k_y\}, \qquad \text{(A5)}$$

$$\hat{m}_i = \{\hat{k}_y\hat{\ell}_z - \hat{k}_z\hat{\ell}_y, \hat{k}_z\hat{\ell}_x - \hat{k}_x\ell_z, \hat{k}_x\hat{\ell}_y - \hat{k}_y\hat{\ell}_x\}, \qquad \text{(A6)}$$

where $\kappa^2 = k_x^2 + k_y^2 + k_z^2$ and $\lambda^2 = \ell_x^2 + \ell_y^2 + \ell_z^2$.

In addition to the tensor harmonics defined above that describe propagating gravitational waves, there are five spatially independent transverse-traceless harmonics that represent nonpropagating waves. These additional harmonics divide naturally into two classes. The first class consists of two time-independent harmonics with polarizations analogous to the propagating + polarization harmonics. These harmonics are defined by

$$Y^{+a}_{ij,0} = \frac{1}{\sqrt{2}}(\hat{y}_i\hat{y}_j - \hat{z}_i\hat{z}_j), \qquad \text{(A7)}$$

$$Y^{+b}_{ij,0} = \frac{1}{\sqrt{6}}(\hat{y}_i\hat{y}_j + \hat{z}_i\hat{z}_j - 2\hat{x}_i\hat{x}_j), \qquad \text{(A8)}$$

where $\hat{x}_i$, $\hat{y}_i$, and $\hat{z}_i$ are the unit vectors in the x, y, and z directions, respectively. The second class consists of three time-independent harmonics with polarizations analogous to the propagating $\times$ polarization harmonics. These harmonics are defined by

$$Y^{\times a}_{ij,0} = \frac{1}{\sqrt{2}}(\hat{y}_i\hat{z}_j + \hat{z}_i\hat{y}_j), \qquad \text{(A9)}$$

$$Y^{\times b}_{ij,0} = \frac{1}{\sqrt{2}}(\hat{x}_i\hat{z}_j + \hat{z}_i\hat{x}_j), \qquad \text{(A10)}$$

$$Y^{\times c}_{ij,0} = \frac{1}{\sqrt{2}}(\hat{x}_i\hat{y}_j + \hat{y}_i\hat{x}_j). \qquad \text{(A11)}$$

This collection of harmonics $Y^{p}_{im,\mathbf{k}}$ provides a complete basis for the symmetric transverse-traceless tensor fields on the three-torus. These harmonics satisfy the orthonormality condition,

$$\delta_{\mathbf{k},\mathbf{k}'}\delta_{p,p'} = \int e^{ij}e^{mn}Y^{p}_{im,\mathbf{k}}Y^{p'}_{jn,\mathbf{k}'}d^3x, \qquad \text{(A12)}$$

where the parameter $p = \{+, \times\}$ represents polarization states for the propagating $\mathbf{k} \neq 0$ harmonics, and $p = \{+a, +b, \times a, \times b, \times c\}$ the polarization states for the nonpropagating $\mathbf{k} = 0$ harmonics.

APPENDIX B: DYNAMICAL FIELD TRANSFORMATIONS

The methods used in this study to solve the initial value problem, and those used to extract the gravitational-wave spectra from the spacetime geometry, are most conveniently expressed in terms of the ADM dynamical fields g_{ij} and K_{ij}. The evolution of the initial data to determine the spacetime geometry, however, is most conveniently performed using the first-order dynamical fields ψ_{ab}, Π_{ab}, and Φ_{iab}. This appendix provides a brief summary of the relationships between these different representations of the dynamical fields.

The transformation between the spacetime metric ψ_{ab} and the standard ADM coordinate representation of the metric is straightforward [23]:

$$\begin{aligned} ds^2 &= \psi_{ab}dx^a dx^b \\ &= -N^2 dt^2 + g_{ij}(dx^i + N^i dt)(dx^j + N^j dt), \end{aligned} \tag{B1}$$

where g_{ij} is the spatial metric on the $t =$ constant hypersurfaces, N is the lapse, and is N^i the shift. The timelike unit normal to the $t =$ constant hypersurfaces is given by $t^a\partial_a = N^{-1}(\partial_t - N^i\partial_i)$ in these ADM coordinates.

The transformation between the extrinsic curvature, K_{ij}, and the first-order dynamical fields Π_{ab} and Φ_{iab} is more complicated. The standard expression for the extrinsic curvature in ADM coordinates is

$$K_{ij} = -\frac{1}{2N}(\partial_t g_{ij} - D_i N_j - D_j N_i), \tag{B2}$$

where D_i is the covariant derivative compatible with the spatial metric, and $N_i = g_{ij}N^j$. This expression can be rewritten by expanding the covariant derivative terms in Eq. (B2) into partial derivatives and metric derivatives:

$$\begin{aligned} K_{ij} = &-\frac{1}{2N}(\partial_t g_{ij} - \partial_i N_j - \partial_j N_i) \\ &-\frac{N^m}{2N}(\partial_i g_{mj} + \partial_j g_{mi} - \partial_m g_{ij}). \end{aligned} \tag{B3}$$

The dynamical fields Π_{ij} and $\Phi_{ija}t^a$ are related to the first derivatives of the spacetime metric ψ_{ab} by

$$\Pi_{ij} = -\frac{1}{N}(\partial_t g_{ij} - N^m\partial_m g_{ij}), \tag{B4}$$

$$\Phi_{ija}t^a = \frac{1}{N}(\partial_i N_j - N^m\partial_i g_{jm}), \tag{B5}$$

in a spacetime where the reference metric is the flat metric given in Eq. (15). Using the expressions for K_{ij} from Eq. (B3) together with the expressions for Π_{ij} and $\Phi_{ija}t^a$ from Eqs. (B4) and (B5), it follows that K_{ij} can be expressed in terms of the first-order dynamical fields:

$$K_{ij} = \frac{1}{2}(\Pi_{ij} + \Phi_{ija}t^a + \Phi_{jia}t^a). \tag{B6}$$

The spacetime evolution code determines the fields ψ_{ab}, Π_{ab}, and Φ_{iab} on a succession of $t =$ constant spacelike hypersurfaces. Given these fields, Eq. (B6) determines K_{ij} in terms of ψ_{ab}, Π_{ab}, and Φ_{iab} on each $t =$ constant hypersurface. On the initial spacelike hypersurface $t = 0$, Eq. (16) sets the lapse to $N = 1$ and the shift to $N^i = 0$, so Eq. (B5) implies that $\Phi_{ija}t^a = 0$ on this initial hypersurface. Therefore, Eq. (B6) leads to the condition $\Pi^0_{ij} = 2K^0_{ij}$ given in Eq. (18). The condition $\Pi^0_{ta} = 0$ in Eq. (17) is a gauge choice that sets the initial time derivatives of the lapse and shift to zero.

APPENDIX C: COVARIANT FIRST-ORDER SYMMETRIC-HYPERBOLIC EINSTEIN SYSTEM

This study uses a covariant representation of the Einstein equations that enforces generalized harmonic gauge conditions [18]. The covariance of this representation facilitates the study of solutions on manifolds represented using multicube coordinate patches, such as the manifold with three-torus spatial slices studied here. All the dynamical fields in this representation are tensors, so they can be transformed in a straightforward way across the interfaces between coordinate patches. The dynamical fields u^α for the first-order symmetric-hyperbolic representation of the Einstein equations used in this study are the collection of tensor fields,

$$u^\alpha = \{\psi_{ab}, \Pi_{ab}, \Phi_{iab}\}, \tag{C1}$$

where ψ_{ab} is the spacetime metric, and the tensors Π_{ab} and Φ_{iab} represent its first derivatives,

$$\Pi_{ab} = -t^c\tilde\nabla_c\psi_{ab}, \tag{C2}$$

$$\Phi_{iab} = \tilde\nabla_i\psi_{ab}. \tag{C3}$$

The covariant derivative $\tilde\nabla_c$ used in these expressions is the one compatible ($\tilde\nabla_c\tilde\psi_{ab} = 0$) with the reference metric $\tilde\psi_{ab}$. This reference metric is also used to define the Jacobians used to transform tensor fields across the boundary interfaces between multicube regions. The vector t^c represents the unit timelike normal to the spacelike hypersurfaces used to perform the evolutions. The lower range of latin indices, e.g., $a, b, c, \ldots$, range over the four spacetime coordinates, while the higher range of indices, e.g., $i, j, k, \ldots$, range over the three spatial coordinates on each $t =$ constant hypersurface. The greek indices, e.g., α, β, γ, range over the 50 components of the dynamical tensor fields u^α. The Einstein equations for these fields can be written in the first-order form

$$\partial_t u^\alpha + A^{k\alpha}{}_\beta(\mathbf{u})\tilde\nabla_k u^\beta = F^\alpha(\mathbf{u}, \tilde{\mathbf{\Gamma}}, \partial\tilde{\mathbf{\Gamma}}), \tag{C4}$$

where the tensors $A^{k\alpha}{}_\beta(\mathbf{u})$ and $F^\alpha(\mathbf{u}, \tilde{\mathbf{\Gamma}}, \partial\tilde{\mathbf{\Gamma}})$ depend in complicated ways on the dynamical fields u^α, the reference connection $\tilde\Gamma^c{}_{ab}$, and its derivatives $\partial_d\tilde\Gamma^c{}_{ab}$. The detailed expressions for this representation are given in Ref. [18].

The spacetime coordinates are determined in the generalized harmonic representations of Einstein's equation by imposing a condition on the difference between the connection $\tilde\Gamma^c{}_{ab}$ associated with the reference metric $\tilde\psi_{ab}$ and the connection $\Gamma^c{}_{ab}$ associated with the physical spacetime metric ψ_{ab}. In particular, the difference between these connections is fixed by a gauge source function H_a:

$$H_a = -\psi_{ad}\psi^{bc}(\Gamma^d{}_{bc} - \tilde{\Gamma}^d{}_{bc}). \tag{C5}$$

(Note that the difference between any two connections is a tensor.) In general, H_a may be any function that depends on the physical metric ψ_{ab} (but not its derivatives) and the reference metric $\tilde{\psi}_{ab}$. The gauge condition used for the numerical evolutions performed in this study is the simple harmonic condition $H_a = 0$.

The generalized harmonic evolution system contains a number of constraints. In particular, the gauge condition Eq. (C5) is in effect a constraint

$$\mathcal{C}_a = H_a + \psi_{ad}\psi^{bc}(\Gamma^d{}_{bc} - \tilde{\Gamma}^d{}_{bc}) \tag{C6}$$

on the dynamical fields. In addition, the equation that defines Φ_{iab}, Eq. (C3), is also a constraint

$$\mathcal{C}_{iab} = \tilde{\nabla}_i\psi_{ab} - \Phi_{iab}. \tag{C7}$$

These primary constraints, $\mathcal{C}_a$ and $\mathcal{C}_{iab}$, satisfy a second-order system of evolution equations as a consequence of the Einstein evolution system Eq. (C4). (See Ref. [18] for details.) This second-order constraint evolution system can be converted to a first-order symmetric hyperbolic system by introducing the secondary constraints,

$$\mathcal{F}_a = t^c\nabla_c\mathcal{C}_a, \tag{C8}$$

$$\mathcal{C}_{ia} = \nabla_i\mathcal{C}_a, \tag{C9}$$

$$\mathcal{C}_{ijab} = 2\tilde{\nabla}_{[i}\mathcal{C}_{j]ab}. \tag{C10}$$

The symmetric-hyperbolic evolution equation for the collection of constraints

$$\mathcal{C}^\alpha = \{\mathcal{C}_a, \mathcal{C}_{iab}, \mathcal{F}_a, \mathcal{C}_{ia}, \mathcal{C}_{ijab}\} \tag{C11}$$

ensures that solutions to the Einstein Eq. (C4) that satisfy the constraints $\mathcal{C}^\alpha$ on an initial surface will satisfy them throughout the evolution of those initial data. Numerical solutions to the equations will of course contain (hopefully small) violations of these constraints. This study monitors the size of these constraint violations by evaluating a norm constructed from the composite constraint $\mathcal{C}_\psi$ defined by

$$\mathcal{C}_\psi^2 = \delta^{ab}(\mathcal{C}_a\mathcal{C}_b + \mathcal{F}_a\mathcal{F}_b) + \tilde{g}^{ij}\delta^{ab}\delta^{cd}\left(\mathcal{C}_{iac}\mathcal{C}_{jbd} + \frac{1}{4}\tilde{g}^{kl}\mathcal{C}_{ikac}\mathcal{C}_{jlbd}\right). \tag{C12}$$

This study evaluates a norm of $\mathcal{C}_\psi$ defined by

$$\|\mathcal{C}_\psi\|^2 = \frac{\int \mathcal{C}_\psi^2\sqrt{g}\,d^3x}{\int \mathcal{N}_\psi^2\sqrt{g}\,d^3x}. \tag{C13}$$

The quantity that appears in the denominator $\mathcal{N}_\psi$ is defined by

$$\mathcal{N}_\psi^2 = \delta^{ab}\delta^{cd}\tilde{g}^{ij}(\partial_i\psi_{ac}\partial_j\psi_{bd} + \partial_i\Pi_{ac}\partial_j\Pi_{bd}) + \delta^{ab}\delta^{cd}\tilde{g}^{ij}\tilde{g}^{kl}\partial_i\Phi_{kac}\partial_j\Phi_{lbd}. \tag{C14}$$

It has been included in the definition of $\|\mathcal{C}_\psi\|$ to provide a dimensionless measure of the fractional errors due to constraint violations in the numerical solutions to the Einstein evolution system.

[1] P. Bizon and A. Rostworowski, Phys. Rev. Lett. **107**, 031102 (2011).
[2] O. J. C. Dias, G. T. Horowitz, and J. E. Santos, Classical Quantum Gravity **29**, 194002 (2012).
[3] S. R. Green, F. Carrasco, and L. Lehner, Phys. Rev. X **4**, 011001 (2014).
[4] S. Ma, L. Lehner, H. Yang, L. E. Kidder, H. P. Pfeiffer, and M. A. Scheel, Phys. Rev. Lett. **136**, 061401 (2026).
[5] S. Rica, arXiv:1608.04293.
[6] S. Galtier and S. V. Nazarenko, Phys. Rev. Lett. **119**, 221101 (2017).
[7] K. Clough and J. C. Niemeyer, Classical Quantum Gravity **35**, 187001 (2018).
[8] S. Galtier, J. Laurie, and S. V. Nazarenko, Universe **6**, 98 (2020).
[9] B. Gay and S. Galtier, Phys. Rev. D **109**, 083531 (2024).
[10] E. Florio and E. P. S. Shellard, Phys. Rev. D **113**, 023534 (2026).
[11] J. Isenberg, in *Springer Handbook of Spacetime*, edited by A. Ashtekar and V. Petkov (Springer-Verlag, Berlin, 2014), pp. 303–321.
[12] J. Isenberg, Classical Quantum Gravity **12**, 2249 (1995).
[13] Z.-P. Peng, L. Lindblom, and F. Zhang, J. Cosmol. Astropart. Phys. 12 (2019) 042.
[14] H. P. Pfeiffer, L. E. Kidder, M. A. Scheel, and S. A. Teukolsky, Comput. Phys. Commun. **152**, 253 (2003).
[15] F. Zhang and L. Lindblom, Gen. Relativ. Gravit. **54**, 130 (2022).
[16] S. Balay, S. Abhyankar, M. F. Adams, S. Benson, J. Brown, P. Brune, K. Buschelman, E. Constantinescu, L. Dalcin, A. Dener *et al.*, Technical Report ANL-21/39—Revision 3.16, Argonne National Laboratory (2021).

[17] C. W. Misner, K. S. Thorne, and J. A. Wheeler, *Gravitation* (W. H. Freeman and Co., San Francisco, 1971).
[18] L. Lindblom, B. Szilágyi, and N. W. Taylor, Phys. Rev. D **89**, 044044 (2014).
[19] L. Lindblom and B. Szilágyi, J. Comput. Phys. **243**, 151 (2013).
[20] F. Zhang and L. Lindblom, Phys. Rev. D **113**, 124012 (2025).
[21] J. R. Dormand, M. E. A. El-Mikkaway, and P. J. Prince, IMA J. Numer. Anal. **7**, 423 (1987).
[22] F. Zhang and L. Lindblom, Using Ricci flow in the construction of homogeneous cosmological models, Phys. Rev. D (to be published).
[23] R. Arnowitt, S. Deser, and C. W. Misner, *Gravitation: An Introduction to Current Research* (W. H. Freeman and Company, San Francisco, 1962).